The stray magnetic fields in Magnetic Resonance Current Density Imaging (MRCDI)

Göksu, Cihan; Scheffler, Klaus; Siebner, Hartwig R.; Thielscher, Axel; Hanson, Lars G.

Published in:
Physica Medica

Link to article, DOI:
10.1016/j.ejmp.2019.02.022

Publication date:
2019

Document Version
Peer reviewed version

The stray magnetic fields in Magnetic Resonance Current Density Imaging (MRCDI)

Cihan Göksu[1] , Klaus Scheffler[2,3], Hartwig R. Siebner[1,4],

Axel Thielscher[1,5†], and Lars G. Hanson[1,5†*]

[1] Danish Research Centre for Magnetic Resonance, Centre for Functional and Diagnostic Imaging and Research, Copenhagen University Hospital Hvidovre, Denmark.

[2] High-Field Magnetic Resonance Center, Max-Planck-Institute for Biological Cybernetics, Tübingen, Germany.

[3] Department of Biomedical Magnetic Resonance, University of Tübingen, Tübingen, Germany.

[4] Department of Neurology, Copenhagen University Hospital, Bispebjerg, Denmark.

[5] Center for Magnetic Resonance, DTU Elektro, Technical University of Denmark, Kgs Lyngby, Denmark.

[†] These authors contributed equally to this work.

* Corresponding Author

Lars G. Hanson, Assoc. Prof.

Danish Research Centre for Magnetic Resonance, Centre for Functional and Diagnostic Imaging and Research, Copenhagen University Hospital Hvidovre, Section 714, Kettegaard Allé 30, 2650 Hvidovre, Denmark.

Tel: + 45-38622977

e-mail: larsh@drcmr.dk

ABSTRACT

Purpose:

MR Current Density Imaging (MRCDI) involves weak current-injection into the head. The resulting magnetic field changes are measured by MRI. Stray fields pose major challenges since these can dominate the fields caused by tissue currents. We analyze the sources and influences of stray fields.

Methods:

First, we supply validation data for a recently introduced MRCDI method with an unprecedented noise floor of ~0.1 nT *in vivo*. Second, we assess the accuracy limit of the method and our corresponding cable current correction in phantoms ensuring high signal-to-noise ratio (SNR). Third, we simulate the influence of stray fields on current flow reconstructions for various realistic experimental set-ups. Fourth, we experimentally determine the physiological field variations. Finally, we explore the consequences of head positioning in an exemplary head coil, since off-center positioning provides space for limiting cable-induced fields.

Results:

The cable correction method performs well except near the cables. Unless correcting for cable currents, the reconstructed current flow is easily misestimated by up to 45% for a realistic experimental set-up. Stray fields dominating the fields caused by tissue currents can occur, e.g. due to a wire segment 20 cm away from the imaged region, or due to a slight cable misalignment of 3 degrees. The noise is increased by 40% due to physiological factors. Minor patient movements can cause field changes of ~40 nT. Off-centered head positioning can locally reduce SNR by e.g. 30%.

Conclusions:

Quantification of stray fields showed that MRCDI requires careful field correction. After cable correction, physiological noise is a limiting factor.

Key words:

magnetic resonance electric impedance tomography, magnetic resonance current density imaging, cable currents, physiological noise

INTRODUCTION

Accurate mapping of the ohmic tissue conductivities at low frequencies (< 10 kHz), and related mapping of electrical current flows *in vivo,* are of high importance for neuroscientific and clinical applications. A first example relates to non-invasive brain stimulation (NIBS) by electrical current injection or electromagnetic induction (transcranial direct current stimulation, alternating current stimulation, and magnetic stimulation; tDCS, tACS and TMS, respectively). These techniques are important for brain research and treatment of neuropsychiatric diseases. A limiting factor is target control and dosing of NIBS techniques, which can be improved by recently developed numerical simulation based on realistic head modelling that requires accurate knowledge of the tissue conductivities, however [1,2]. Also, the conductivity maps can improve electro- and magneto-encephalography (EEG, MEG) source localization techniques [3], and can provide useful information for tumor diagnosis as the ohmic conductivity depends on the pathological state of the tissue [4].

Magnetic resonance current density imaging (MRCDI) [5] and electrical impedance tomography (MREIT) [6] are methods to map current flow and ohmic conductivity distributions respectively, and their *in vivo* human brain implementations have recently been demonstrated. In both methods, weak electrical currents (1-2 mA) that are synchronized with an MR sequence are injected into the head via scalp electrodes. The current induces a magnetic field, and the component $\Delta B_{z,c}$ that is parallel to the scanner field modulates the phase of the acquired MR signal accordingly. Therefore, the current-induced magnetic field $\Delta B_{z,c}$ can be determined from MR measurements, and the current flows and ohmic conductivities can be derived by means of recently developed reconstruction techniques [7–13]. However, accurate current flow and conductivity reconstructions require sensitive $\Delta B_{z,c}$ measurements with high accuracy and precision.

Recently, Kasinadhuni *et al* [14] reported the first *in vivo* $\Delta B_{z,c}$ and current flow measurements inside human brain at high spatial resolution. However, the field measurements did not match simulations well, and were not consistent across subjects. We subsequently reported consistent and unambiguous *in vivo* $\Delta B_{z,c}$ and current flow measurements inside the human brain with an unprecedented sensitivity of ~0.1 nT, based on a steady-state free precession free induction decay (SSFP-FID) sequence [15]. Our study demonstrated that currents flowing in the feeding electrode cables can severely influence magnetic field measurements and cause highly inaccurate current flow reconstructions unless corrected. The originally proposed MRCDI method [16], which involves separate measurement of orthogonal components of the current-induced field and reconstruction of currents based on Ampere's Law, is robust against stray fields, but is likely impossible in practice as the method requires subject rotation, which deforms the cable paths. Alternatively, these influences can be avoided by using a conductivity reconstruction based on the second derivative of $\Delta B_{z,c}$ measurements [17]. This method unfortunately involves a severe signal-to-noise-ratio (SNR) compromise and is therefore currently not

applicable for human *in vivo* brain MRCDI, so it is not considered further here. In addition to establishing the significance of cable current correction, we found noise to be amplified relative to a prior phantom study with relaxation parameters matched to human brain tissue [18]. This demonstrates that physiological variation (for example due to motion, respiration, pulsation, or blood flow) severely reduces the sensitivity of MRCDI measurements. Taken together, the prior studies show that MRCDI and MREIT measurements are highly susceptible to spurious field variations. This is expected considering that the current-induced field changes are in the order of nT, which is approximately 10^{-9} times smaller than the main magnetic field. It is extraordinary that consistent and useful results can nevertheless be obtained, but it is clear that stray field variations need to be better characterized and carefully accounted for to make MRCDI and MREIT results accurate.

In this study, we first characterize our SSFP-FID implementation using phantoms with no physiological variation and the previously proposed correction method for cable currents. This establishes the limits of sensitivity when the stray fields are controlled. Second, we explore the influence of cable currents by stray field simulations for different cable placements and alignments. Third, we experimentally characterize slow field drifts due to temperature variations and other scanner instabilities caused by hardware imperfections. Fourth, we further explore the measured field drifts due to physiological variation caused by respiration, pulsation, and unintentional motion. This is supported by experiments performed during both rest and intentional jaw movements. Finally, we test the signal-to-noise-ratio (SNR) compromise for two different experimental set-ups with the head centered or off-centered in an exemplary MR coil, as the off-centered set-up allows for choosing cable paths that reduce the influence of cable currents.

THEORY

SSFP-FID Magnetic Resonance Current Density Imaging (MRCDI)

In MRCDI, an external current is generated by a current source, filtered to avoid RF interferences, and injected into the human head via scalp electrodes (Fig. 1a). The component $\Delta B_{z,c}$ of the current-induced magnetic field that is parallel to the scanner field modulates the phase of the transverse magnetization, depending on the phase sensitivity m_{seq} of the MR sequence. The phase sensitivity depends on sequence parameters and can be simulated by integrating Bloch equations expressed in terms of 3D rotation matrices [18–20]. MRCDI measurements based on the SSFP-FID sequence employ alternating currents and identical in-phase excitation pulses separated by the repetition time T_R to create two alternating steady states with different current-induced phases ($\measuredangle\mu^+$ for positive (+) and $\measuredangle\mu^-$ for negative (−) currents; Fig. 1b). The phases of the acquired MR images can then be used to calculate current-induced magnetic field images from $\Delta B_{z,c} = (\measuredangle M^+ - \measuredangle M^-)/m_{seq}$ for weak currents. In order to prevent low-bandwidth-related artifacts and to increase the robustness against

physiological variation, multi-gradient-echo readouts are preferred [15]: Individual phase difference images acquired from each gradient echo are used to calculate corresponding $\Delta B_{z,c}$ images. Then, each of the calculated $\Delta B_{z,c}$ images are weighted by its inverse variance and the images are combined [18,21].

The combined $\Delta B_{z,c}$ measurements can be used to reconstruct the current flow distribution J_{rec}, called the "Projected Current Density" in [10]:

$$J_{rec} = J_0 + \frac{1}{\mu_0}\left(\frac{\partial(\Delta B_{z,c} - \Delta B_{z,c}{}^0)}{\partial y}, -\frac{\partial(\Delta B_{z,c} - \Delta B_{z,c}{}^0)}{\partial x}, 0\right) \quad (1)$$

J_0 and $\Delta B_{z,c}{}^0$ are the current flow and magnetic field for a given uniform conductivity distribution, which can be calculated by means of FEM simulations (finite element modelling, [2]), and μ_0 is the permeability of free space.

Stray magnetic fields due to the cable currents and a correction method

An accurate mapping of the current flow and ohmic conductivity distribution requires sensitive measurement of uncontaminated $\Delta B_{z,c}$ fields caused by tissue currents. In an MRCDI experiment, the currents are delivered via leads connecting a current source to the scalp electrodes, and these cable currents induce an additional field change depending on the geometry of the experimental set-up. These spurious field changes can easily be stronger than the relevant field contributions induced by tissue currents, and they need to be corrected ([15]; Figure 2a).

In a prior study, we proposed a correction method ([15]; Fig. 2) based on imaging of the cable paths and Biot-Savart simulations. The cables are covered (Fig. 2) with a paste such as Play-Doh (Hasbro Inc., RI, USA) or a rubber coating that can be imaged by an ultra-short echo time (UTE) sequence due to their hydrogen content and relative softness. The two cable segments connecting the anode and cathode electrodes to the current source are localized within the imaged region by manual tracking, starting from the midpoints of the rubber electrodes and ending where the cable segments merge. The current-induced magnetic fields due to cable currents are then calculated using the Biot-Savart law $\vec{B}_{cables} = \frac{\mu_0 I}{4\pi} \cdot \int \frac{1}{r^2} \overrightarrow{dl} \times \vec{a}_r$, where r is the distance between a source point along the cable path and an observation point in the imaging region, $\vec{a}_r$ is the corresponding unit vector from the source point to the observation point, I is the applied current strength, and $\overrightarrow{dl}$ is the infinitesimal vector along the cable path over which integration is done. The component of $\vec{B}_{cables}$ that is parallel to the scanner field is then subtracted from the $\Delta B_{z,c}$ measurements to correct for spurious field contributions.

The $\Delta B_{z,c}$ measurements also stray due to the slow field drifts induced by scanner instability, and physiological factors. These error sources are evaluated, but their correction methods are not addressed in this study.

METHODS

1) SSFP-FID MRCDI: Method validation by means of phantom experiments

In a previous study [15], we have validated an SSFP-FID MRCDI method in humans *in vivo* by means of checking the linear dependence of the $\Delta B_{z,c}$ measurements on the applied current strength. We also validated our cable current correction method by comparing the $\Delta B_{z,c}$ measurements and simulations. The currents were not injected into the head, but flowing in a cable that was placed around it. The simulated fields were subtracted from the measurements and the residuals were compared with control experiments without currents.

To explore the correction accuracy, we supplement here with phantom experiments conducted similarly using a 3T scanner (Magnetom Prisma, Siemens Healthcare, Erlangen, Germany). They were based on SSFP-FID with multi-gradient-echo readouts to demonstrate its performance under no physiological variation and to ensure high signal-to-noise ratio. The experiments were performed using a spherical FBIRN gel phantom 18 cm in diameter and with relaxation parameters approximately matched to the human brain tissue [22], with an image matrix 112x90, a voxel size 2x2x3 mm^3, and a tip-angle $\alpha=30^\circ$. The currents were not injected inside the phantom, and its electrical properties are thus insignificant.

- *Linear dependence of current-induced fields on the current strength*

In order to verify the linear dependence of the measured $\Delta B_{z,c}$ on the applied current strength, SSFP-FID experiments were performed with T_R=120 ms, number of measurement repetitions N_{meas}=12, and number of gradient-echoes N_{GE}=7 for four different current strengths I_c=[0, 0.33, 0.66, 1] mA in a random order (4x12=48 measurements in total). For each measurement, average $\Delta B_{z,c}$ values were extracted from a region-of-interest (ROI), and linear regression models were fitted to the extracted values as a function of I_c.

- *Correction for stray magnetic fields due to cable currents*

SSFP-FID measurements using different acquisition schemes potentially differ by their sensitivity to $\Delta B_{z,c}$ and physiological noise, as explored later. In order to verify the correction method under no physiological variation, four such sets of experiments, each with total scan time of T_{tot} = 3.6 mins, were performed:

Exp 1: T_R=60 ms, N_{GE}=5, T_E=[5.4, 13.6, 21.8, 30.0, 38.1] ms, and N_{meas}=20 averages to increase the signal-to-noise ratio.

Exp 2: T_R=80 ms, N_{GE}=5, T_E = [7.5, 19.7, 31.9, 44.0, 56.1] ms, and N_{meas}=15.

Exp 3: T_R=100 ms, N_{GE}=7, T_E = [7.1, 18.7, 30.3, 41.8, 53.4, 64.9, 76.4] ms, and N_{meas}=12.

Exp 4: T_R=120 ms, N_{GE}=7, T_E = [8.3, 22.4, 36.5, 50.6, 64.7, 79.9, 93.2] ms, and N_{meas}=10.

Before each of the experiments, a high-resolution structural image was acquired using the Pointwise Encoding Time reduction with Radial Acquisition (PETRA) sequence [23] with number of slices N_{sli}=320, image matrix 320x320, voxel size 0.9x0.9x0.9 mm^3, $\alpha=6^\circ$, T_R = 3.61 ms, T_E = 0.07 ms, inversion time T_I = 0.5 s, and bandwidth 359 Hz/pixel. The PETRA images were used to manually delineate the cable paths that were then used for Biot-Savart simulations. The Biot-Savart simulations were directly compared with the $\Delta B_{z,c}$ measurements, and the difference between the simulations and the measurements were evaluated. The difference images (ideally being zero) were qualitatively compared with control experiments with no currents. The accuracy was further assessed by means of noise floor comparisons: Gaussian distributions were visually found to be accurate and were fitted to the difference and to the control measurements, and the standard deviations of the fitted distributions were calculated. This provides more robust estimates than the directly calculated standard deviations, which are larger, but the differences were small in practice.

2) Simulations of the stray fields due to the cable currents

Currents in a straight wire induce magnetic fields that are orthogonal to the wire only, and their magnitude scales inversely with the distance between the wire and the observation point. In a standard MRCDI experiment, the cables are therefore preferably placed in parallel with the scanner field and as far away as possible from the head to minimize the effects of stray magnetic fields due to the cable currents. However, the commercially available electrode cables approved for clinical use are restricted in length to ensure their safety in the MRI environment. Severe burns from heating of cables and tissue may be caused by coupling to the radio frequency (RF) transmitter system of the scanner [24]. The risk is particularly high for long uninterrupted stretches of cable, and short cables are therefore normally preferred. This makes it difficult to practically ensure that cable segments that are not parallel to the scanner's static field occur only far away from the imaged region to avoid significant unwanted field changes. The currents in electrode pads also contribute to stray fields.

Here, we performed Biot-Savart simulations for the cables as described in the theory section while subdividing each linear segment into 1000 pieces. The field changes due to a wire segment that was orthogonal to the main field and placed d = [4–16] cm away along the z-direction from the imaging region were calculated. We also simulated the field changes due to misalignment by θ = [0–40] degrees of the cable segments that are ideally parallel to the main field (Fig. 2c; d and θ intervals were selected considering the physical constraints of an exemplary electrode cable (neuroConn GmbH,

Ilmenau, Germany) and a head coil (32 Channel SENSE HC, Phillips Healthcare, Amsterdam, Netherlands) that were both used in [14]). Such misalignment is difficult to avoid in practice. We used methodology similar to our prior study [15], where we simulated current-induced magnetic fields based on a realistic head model to demonstrate the influences of the spurious fields due to the cable currents in current density reconstructions. The head model was created based on T_1- and T_2-weighted structural scans. It consists of five tissue compartments, which are gray matter (GM), white matter (WM), cerebrospinal fluid (CSF), skull, and scalp. Isotropic ohmic conductivities were assigned to the tissues (WM: 0.126 S/m, GM: 0.275 S/m, CSF: 1.654 S/m, bone: 0.010 S/m, scalp: 0.465 S/m). The scalp electrode positions were determined from the structural images. The electrode pads were modelled as disks (5 cm in diameter and with 5 mm thickness) with a conductivity of 1.0 S/m, and the currents flowing in the electrode pads were included in the simulations. In this study, we used the current-induced field simulations of the first subject in [15], and proceeded to reconstruct currents from the sum of simulated relevant and spurious current-induced fields, and from the relevant fields only, to demonstrate the deviations for various realistic d and θ values.

3) Experimental characterization of the temporal variation of the measured fields

The slow field drifts due to scanner instability, temperature variation, and physiological variation are intrinsic causes of measurement variance. In an MRCDI experiment aiming to measure the tiny field changes due to tissue currents (~nT scale), the influence of physiological variations and subject motion can become important. Here, we explore these field changes by three sets of single-slice echo planar imaging (EPI) experiments [25]:

- Phantom: No physiological variation.
- Human *in vivo*: With physiological variation. Subject performs no intentional motion.
- Human *in vivo*: With physiological variation. Subject performs intentional jaw movements to exemplify common movement.

The EPI measurements with acquisition matrix 52x64, voxel size 3.5x3.5x5 mm^3, $\alpha=20^\circ$, T_R = 60 ms, T_E = 30 ms, and bandwidth 1150 Hz/pixel were repeated N_{meas} = 4096 times. The first 96 measurements were discarded to enter a steady-state condition. The phase of the measured MR signal in a representative voxel was measured for every repetition. The average phase of the first 100 measurements was taken as a reference, and subtracted from each of the measurements to observe the temporal phase variation $\Delta(\measuredangle M(t))$, which was then used to calculate the field variation $\Delta B_z(t) = \Delta(\measuredangle M(t)) / \gamma T_E$ where γ is the proton gyromagnetic ratio 42.58 MHz/T, and the field spectral density $\Delta B_z(f)$ with a bandwidth of 16.7 Hz ($\Delta B_z(f)$ is the Fourier transform of the windowed $\Delta B_z(t)$).

4) Signal-to-noise ratio (SNR) dependence on head positioning in the RF coil

Due to the restricted size and geometry of modern multi-channel MR head coils, the electrode cable segments that are not parallel to the scanner field cannot be placed sufficiently far from the imaging region to avoid significant field contributions. When the cables leave the electrodes in the inferior direction (towards the feet), they may physically interfere with body positioning, and be affected by chest movements. This positioning is not considered further here. When the electrode cables instead leave the coil through a hole in the top of an otherwise closed head coil, the stray fields can be reduced by positioning the coil more superior than normally recommended (off-center positioning), but with a compromise in MR SNR.

To evaluate the SNR loss, we performed MR experiments in a 3T MR scanner (Achieva, Phillips Healthcare, Amsterdam, the Netherlands) with an exemplary head coil, also used by Kasinadhuni *et al* [14] (32 Channel SENSE HC, Phillips Healthcare, Amsterdam, Netherlands). The experiments were based on a 3D, T_1-weighted, fast low angle shot (FLASH) sequence with number of slices N_{sli} = 200, image matrix 256x256, voxel size 0.8x0.8x1 mm^3, $\alpha = 8^{\circ}$, T_R = 6.6 ms, and T_E = 3.1 ms. The experiments were repeated for two positions of the head in the RF coil, centered vs. off-centered (approximately ~5 cm displacement). The SNR of the measurements were calculated in three different slices covering the upper, middle, and bottom parts of the brain [26], and directly compared for the two cases.

All human experiments were performed on a healthy volunteer. The subject was screened for contraindications to MRI and transcranial brain stimulation, and written informed consent was obtained prior to the experiments. The study complied with the Helsinki declaration on human experimentation and was approved by the Ethics Committee of the Capital Region of Denmark (H16032361).

RESULTS

1) SSFP-FID MRCDI: Method validation by means of phantom experiments

- *Linear dependence of current-induced fields on the current strength*

Fig. 3a shows the 3D visualization of the leads with cable coatings and the phantom. The signal acquired from the cable coating is sufficient for accurate manual tracking of the cables. The current-induced field measurements (Fig. 3b,c) agree well with the right-hand rule. The measured field strength increases with higher currents as expected. No significant artifacts are observed in field measurements and MR magnitude images. Linear regression models fitted to the average field measurement in a region-of-interest (ROI) demonstrate a good linear dependence of the measurements on the applied current strength. The results are highly significant with an almost zero intercept $\beta_0 = 0 \mp 0.03$ nT, and with a slope $\beta_1 = 0.61 \mp 0.06$ nT/mA ($F_{1,46} = 104$, $p<0.001$).

- *Correction for stray magnetic fields due to cable currents*

Fig. 4 shows no clear quality differences in MR magnitude images for T_R=[60, 80, 100, 120] ms (1st row), and no artifacts are observed. The control measurements without currents (2nd row) exhibit noise floors of $\sigma_{\Delta B_{z,c}}$=[46, 46, 54, 58] pT. The cable current correction error (the difference between measured and simulated current-induced field images; 3rd row) exhibit slightly higher variations of $\sigma_{\Delta B_{z,c}}$=[123, 88, 109, 67] pT, which is likely due to small inaccuracies in cable tracking. This is corroborated by relatively high correction errors in close proximity to cables, especially for T_R = 60 and 120 ms. The correlation R^2 between the field simulations and measurements are higher than 97% for each of the measurements.

2) Simulations of the stray fields due to the cable currents

Figure 5 illustrates the simulations of probable stray magnetic fields for two cases, a finite wire placed d = [4–16] cm away from the imaging region, and cable misalignments of θ = [0–40] degrees (Fig. 2c). The stray fields for d<12 cm are seen to severely deviate from the current-induced fields without any stray field (d→ ∞; first row and first column). The coefficient of determination R^2 drastically drops down to near zero for d = 10 cm (for d<10 cm R^2 slightly increases, which is misleading, since the stray fields start to dominate and appear similar to the relevant fields, but with an inverse polarity). A misalignment angle θ_y in the y-z plane influences the stray fields similar to the distant wire case: R^2 drastically drops to near zero for $\theta_y = 15^\circ$. A misalignment angle θ_x in the x-z plane causes the stray field to shift spatially in the x-direction. Even a small misalignment of $\theta_x \sim 10^\circ$ can cause severe stray fields with a more than 20% drop in R^2. Field deviations that are in the order of the best demonstrated sensitivity level of 0.1 nT *in vivo* (for a total scan time of 9 mins) can occur due to a 17 cm long wire placed as far as 20 cm away from the region of interest, or due to a slight cable misalignment of $\theta > 3^\circ$ (simulated with no wire segments between the anode and cathode electrodes to demonstrate the influence of misalignment only).

Current flow simulations (Figure 6) show no significant loss in reconstruction accuracy for d >8 cm. However, R^2 drops drastically for d < 8 cm, and erroneously high current density estimates appear in the entire region between the electrodes (red dashed rectangle). Cable misalignment mostly influences the field estimates near electrodes and causes misestimation of the tissue currents. Significant drops in R^2 (>10%) occur for misalignments more than 20° for d = 16 cm. However, ensuring a large distance (d = 16 cm) between cables and imaging region is practically difficult, and higher deviations occur for smaller misalignments in case of closer proximity between cables and imaging region. In an exemplary realistic experimental set-up with d = 12 cm, $\theta_x = 10^\circ$, and $\theta_y = 20^\circ$, current flows are misestimated approximately 45% near electrodes and 10% in inner brain regions. The spatial variation of the relative error for various d and θ values is shown in supplementary Figure S1. The error is

calculated as $\left(J_{rec}^{stray} - J_{rec}^{ref}\right)/J_{rec}^{ref}$, where J_{rec}^{ref} is the reference current flow image reconstructed from current-induced field simulations without stray fields, and J_{rec}^{stray} is with stray fields.

3) Experimental characterization of the temporal variation of the measured fields

Figure 7 demonstrates inevitable random noise variations, and linearly varying field drifts due to hardware instability. The linear field drifts can be corrected by fitting a linear regression model to the measurements. In phantom measurements, the noise spectral density of the corrected field variations in a randomly selected representative voxel is uniformly distributed over all frequencies, similar to white noise. The noise amplitude in the selected voxel is 6.7 nT. In human experiments, the spectral density plots demonstrate noise peaks due to respiration (around 0.2 Hz) and pulsation (0.9 Hz). The noise amplitude in the selected voxel is 9.4 nT, and this demonstrates ~40% increase due to the physiological factors. The noise peaks due to pulsation are higher in the slices covering the lower parts of the brain as expected. There are no obvious noise floor differences between measurements at rest and with occasional jaw movements. However, sudden drastic field changes of ~40 nT occur during jaw movement. Such high field changes (4 times higher than the general noise level) can severely decrease MRCDI measurement accuracy unless corrected. The specific values above will vary between measurements and subjects, and are provided as representative examples only.

4) Signal-to-noise ratio (SNR) dependence on head positioning in the RF coil

The comparison of MR SNR measurements for centered and off-centered positioning (supplementary Figure S2) demonstrates average SNR losses of 12%, 13% and 27% in slices covering the bottom, middle, and top parts of the brain in case of off-centered head positioning. Local losses exceed 20%, 20%, and 30% in the 3 slices respectively. Since noise floors in MRCDI experiments scale inversely with the SNR of MR magnitude images [27], this demonstrates the importance of centered head-positioning in an MRCDI experiment, which restricts the space between the cables and head and thus sets a lower limit for the influence of stray fields.

DISCUSSION AND CONCLUSIONS

We tested our MRCDI SSFP-FID implementation by means of phantom experiments ensuring high SNR, and provided important supplementary validation data demonstrating the linear dependency of the current-induced field $\Delta B_{z,c}$ on the applied current strength. Using different sets of MR acquisition parameters, we also tested our correction method for spurious fields caused by cable currents, and explored its accuracy. Independent of the acquisition method, the findings demonstrate that our correction method exhibits an overall good performance except for regions in close proximity of

cables (less than 3 cm distance), as slight inaccuracies in tracking of their paths severely influence the field estimates near cables.

We explored the consequences of uncorrected stray magnetic fields due to cable misalignments by means of Biot-Savart simulations. The results demonstrate that a 17 cm long wire (exemplarily given for a realistic MRCDI experiment) placed as far away as 20 cm, or a slight misalignment of 3° will cause stray fields around 0.1 nT, i.e. in the order of the sensitivity level of our MRCDI method. Ensuring near-perfect alignment of the electrode cables, and sufficient distance with available clinically approved brain stimulation devices is practically very challenging. Considering a realistic experimental set-up, uncorrected stray magnetic fields can easily cause misestimation of current flows by 45% near electrodes and 10% in inner brain regions. Cable currents therefore need to be well corrected. These findings likely explain the unexpected and inconsistent results in the first reported human brain MRCDI study [14]. Stray fields can also be caused by electromagnetic induction due to movement of highly conductive cable loops. However, modern stimulators accommodate safety resistors and current control rendering induced cable currents insignificant.

Another important factor affecting the sensitivity of an MRCDI experiment is the SNR of the MR measurements. The influence of cable currents can be minimized by ensuring sufficient space between the cables and the head, which for semi-closed head coils can be realized by positioning the coils more superior than normally recommended. For an exemplary head coil used for MRCDI [14], we observed that off-center positioning (approximately 5 cm) causes around 27% average SNR decrease for a slice covering the top part of the brain (maximally around 30%). This drop is too severe to warrant reduction of cable current influences by this strategy. The losses may be different for other coils and off-center distances, but the trend is expected to be common for sensitive many-channel head coils designed to be tight-fitting.

Apart from the cable currents, another source of problematic stray fields and phase instability is the physiological variation due to breathing, pulsation, and other subject motion. Tissue eddy currents, pulsation, chest movement, and oxygenation changes in the breathed air all contribute to this [28]. Comparing the noise in phantom and human experiments, a 40% increase due to physiological noise is observed. Jaw movement experiments demonstrate that sudden instant motion, e.g. due to brief swallowing, discomfort, or involuntary twitches, do not influence the overall noise much, but it can cause drastic sudden field changes of e.g. ~40 nT. These stray fields are much stronger than the target current-induced fields of ~1 nT, but our acquisition scheme (MR signals with (+) and (-) currents acquired subsequently for each k-space line) is robust against slow field changes and performs well in detecting tiny current-induced field changes. However, if spurious field changes occur during the acquisition of k-space center, for example, then the sensitivity of the MRCDI measurement may be severely reduced.

Optimum MRCDI experimental set-up

The optimum MRCDI experimental set-up requires perfect alignment of the electrode cables parallel to the scanner field. Mechanically stable and rigid cable paths may solve this problem. In addition, any cable segment that is not parallel to the scanner field needs to be placed as far as possible from the head. This will be feasible only with specially designed longer electrode cables. However, long cables more easily couple with the RF system of the scanner and can cause reduced coil sensitivity and/or severe burns [24], unless the cables are specially designed to avoid such problems. Another crucial aspect is to restrain head movement by support with cushions or other fixation techniques. In addition to the electrode cables, the current flow in the electrode pads also contributes to the spurious fields. The commercial brain stimulation devices use rubber electrode pads, and their electromagnetic properties influence the local sensitivity to field changes and therefore also the sensitivity to spurious fields. The electrodes are placed inside sponges soaked in saline or attached to the scalp via conductive gels. Obtaining a uniform electrode-skin impedance is practically not possible with any of the methods, resulting in a variable current distribution in the electrodes that it is difficult to account for even with detailed forward models. Therefore, regions near electrodes are always susceptible to spurious field changes.

Improving cable correction strategies

Our method that involves cable path delineation based on UTE imaging of cable coating perform well both in phantoms and *in vivo*. The technique is robust against the chemical shifts of coatings, as the bandwidth per voxel is very high. This technique's main drawback is manual tracking that can be ameliorated using automatic path extraction algorithms. Also, distant regions with poor imaging gradient linearity can cause slight shifts and geometrical distortions, which will result in inaccurate cable path delineations, and thus inaccurate field estimates.

Prior studies and future work

MRCDI experiments in phantoms, animals, and in human lower extremities [29–31] were already performed and promising current flow and conductivity reconstructions were obtained. However, high sensitivity was achieved by using stronger currents that are not applicable for the human brain *in vivo*. To our knowledge, only three prior studies reported current-induced magnetic field measurements in human brain *in vivo* [14,15,32]. In [32], standard field mapping sequences were employed and the achieved sensitivity is not sufficient for obtaining high resolution current-induced field maps. In [14], the achieved sensitivity is sufficient for such mapping, but the field measurements and reconstructed current flows were ambiguous and inconsistent across subjects. Spatial distributions of the current-induced field and current flow measurements seem to be highly contaminated by the spurious field changes due to the cable currents. An extension [33] to [14] reported the first high resolution conductivity distribution estimates reconstructed from the same current flow data sets used in [14]. In

these prior studies, contributions of the cable currents to the measured fields were not addressed. Interestingly, both the current-induced field measurements and the reconstructed current flow maps exhibit similar spatial distributions as our simulations of the stray field contributions shown here (Fig. 5 and 6). The prior studies were therefore likely severely influenced by cable currents. The latest *in vivo* measurements of current-induced magnetic fields in the human brain were reported in our previous study [15], where we showed unambiguous field and current flow measurements, consistent across different subjects and with a so far best sensitivity of 0.1 nT for 9 minutes measurement, achieved using optimized MR sequence parameters and echo-weighting to maximize the method's field sensitivity [15,18]. The field measurements still exhibited unexpected variations near electrode regions, which were likely due to slight inaccuracies in tracking of cable paths and thus imperfect correction of the cable currents. The achieved sensitivity of 0.1 nT is likely still not sufficient for human brain MREIT, and experimental set-ups and spurious field correction methods need further improvement for high-quality mapping of current flow and conductivity in the human brain *in vivo*.

Future studies might aim to account for physiological noise to increase sensitivity, e.g. by means of navigator echoes [34]. According to the results in this study, a sensitivity increase of up to 40% may be feasible. An optimized MRCDI experimental set-up with longer cables may help to ameliorate the impact of cable currents, but careful attention must be paid to RF heating and other safety aspects. The use of ultra-high field MR scanners can further increase the sensitivity, but it also brings practical challenges e.g. worse shimming and additional RF safety concerns.

Conclusions

Prevention and correction of stray fields is crucial when magnetic fields induced by tissue currents are mapped. Our correction method reduces the problems strongly, and is sufficient except near cables and electrodes. Further sensitivity improvements using optimized experimental set-ups, and better handling of spurious field changes in MRCDI may render the technique clinically feasible for high-resolution current flow and conductivity mapping of the brain *in vivo*, which is important for various neuroscience applications.

ACKNOWLEDGEMENTS

This study was supported by the Lundbeck foundation (grant R244-2017-196 to Axel Thielscher).

FIGURE CAPTIONS

Figure 1. (a) Experimental set-up for MRCDI and MREIT. The electrical current source for transcranial current stimulation generates current waveforms in synchrony with the employed MRI sequence. The currents are filtered to avoid RF interference, transmitted to the subject inside the MR scanner room via cables, and injected into the subject's brain via scalp electrodes. (b) Schematic diagram of the MRCDI method based on SSFP-FID (please see [15,18] for details).

Figure 2. (a) The experimental set-up for cable current correction. The electrode cables are covered with a material (Play-Doh, Hasbro Inc., RI, USA) that is imaged with a UTE MR sequence. (b) UTE images show rubber electrodes attached to the scalp via conductive adhesive gels (bright layers in between electrodes and skin) and cable coatings well, and allow for manual tracking of cable paths. (c) Simulation set-ups for cable-current-induced stray fields. The simulations were performed for a realistic head of width L = 17 cm. Distance variation: (i) A wire segment 17 cm in length placed distance d away from the imaging region. The connecting cables closing the loop were placed parallel to the scanner's field (z-direction), and thus do not contribute to the measurable field. Angle variation: The connecting cables were misaligned (ii) angle θ_y in the y-direction or (iii) angle θ_x in the x-direction.

Figure 3. (a) 3D visualization of the phantom and the cables covered with Play-Doh. (b) Linear dependence of the current-induced magnetic fields $\Delta B_{z,c}$ on the applied current strength I_c = [0, 0.33, 0.66, 1] mA. (c) The average $\Delta B_{z,c}$ values were extracted from a region-of-interest (ROI; black dashed rectangles) chosen in the $\Delta B_{z,c}$ images. The images agree well with the right hand rule and show no significant artifacts.

Figure 4. Stray field correction for cable-current-induced fields. First row: The MR magnitude images show no artifacts or quality differences for four different repetition times T_R = [60, 80, 100, 120] ms. Second row: Control experiments without currents. Third row: The cable current correction error (the difference between measured and simulated current-induced field images) for 1 mA current flowing in the cables wrapped around the phantom. The erroneous field measurements near cables are due to slight inaccuracies in cable tracking (black dashed ellipsoids).

Figure 5. Biot-Savart simulations of the cable-current-induced stray fields. (a) The desired $\Delta B_{z,c}$ image without stray fields (left) is compared with $\Delta B_{z,c}$ images with stray fields for four different simulations in which the wire segment is placed d = [4, 8, 12, 16] cm away from the imaging region (first row). $\Delta B_{z,c}$ images for cable misalignments θ_y = [10, 20, 30] degrees in y-direction (second row)

and θ_x = [10, 20, 30] degrees in x-direction (third row). Simulations were performed for d = 16 cm. (b) The coefficients of determination between the stray magnetic fields and the desired $\Delta B_{z,c}$ image without stray fields.

Figure 6. Projected current density images J_{rec} reconstructed from the Biot-Savart simulations in Figure 5.

Figure 7. The recorded field variations. First column: MR magnitude images. Second row: Measured temporal field variation $\Delta B_z(t)$ (blue) and the fitted linear regression model (red). Third column: The spectral density $\Delta B_z(f)$ of the corrected field variations (obtained by subtracting the fit from $\Delta B_z(t)$ measurements). (a) Phantom measurements exhibit random noise variations and a linear field drift only. (b) Human brain experiments. All measurements exhibit noise peaks and higher harmonics of those due to respiration and pulsation in spectral density plots. The impact of pulsation is stronger in the slices covering the lower parts of the brain. In the experiments with jaw movements, sudden fields variations are observed (black dashed ellipsoids).

References

[1] Thielscher A, Antunes A, Saturnino GB. Field modeling for transcranial magnetic stimulation: A useful tool to understand the physiological effects of TMS? Proc. Annu. Int. Conf. IEEE Eng. Med. Biol. Soc. EMBS, 2015, p. 222–5. doi:10.1109/EMBC.2015.7318340.

[2] Opitz A, Paulus W, Will S, Antunes A, Thielscher A. Determinants of the electric field during transcranial direct current stimulation. Neuroimage 2015;109:140–50.

[3] Mosher JC, Leahy RM, Lewis PS. EEG and MEG: Forward Solutions for Inverse Methods. IEEE Trans Biomed Eng 1999;46:245–59.

[4] Fear EC, Hagness SC, Meaney PM, Okoniewski M, Stuchly MA. Enhancing Breast Tumor Detection with Near-Field Imaging. IEEE Microw Mag 2002;3:48–56.

[5] Joy M, Scott G, Henkelman M. In vivo Detection of Applied Electric Currents by Magnetic Resonance Imaging. Magn Reson Imaging 1989;7:89–94.

[6] Ider YZ, Birgül Ö. Use of the magnetic field generated by the internal distribution of injected currents for Electrical Impedance Tomography (MR-EIT). ELEKTRİK 1998;6:215–25.

[7] Seo JK, Woo EJ. Magnetic Resonance Electrical Impedance Tomography. Soc Ind Appl Math 2011;53:40–68.

[8] Sadighi M, Göksu C, Eyüboğlu BM. J-based Magnetic Resonance Conductivity Tensor Imaging (MRCTI) at 3 T. Annu. Int. Conf. IEEE Eng. Med. Biol. Soc. - EMBC, 2014, p. 1139–42.

[9] Ider YZ, Birgül Ö, Oran ÖF, Arıkan O, Hamamura MJ, Müftüler T. Fourier transform magnetic resonance current density imaging (FT-MRCDI) from one component of magnetic flux density. Phys Med Biol 2010;55:3177–99. doi:10.1088/0031-9155/55/11/013.

[10] Park C, Lee B Il, Kwon OI. Analysis of recoverable current from one component of magnetic flux density in MREIT and MRCDI. Phys Med Biol 2007;52:3001–13. doi:10.1088/0031-9155/52/11/005.

[11] Seo JK, Kwon O, Woo EJ. Magnetic resonance electrical impedance tomography (MREIT): conductivity and current density imaging. J Phys Conf Ser 2005;12:140–55. doi:10.1088/1742-6596/12/1/014.

[12] Eyüboğlu BM. Magnetic Resonance-Electrical Impedance Tomography. Wiley Encycl. Biomed. Eng., vol. 4, 2006, p. 2154–62.

[13] Kwon OI, Sajib SZ, Sersa I, Oh TI, Jeong WC, Kim HJ, et al. Current Density Imaging During Transcranial Direct Current Stimulation Using DT-MRI and MREIT: Algorithm Development and Numerical Simulations. IEEE Trans Biomed Eng 2016;63:168–75. doi:10.1109/TBME.2015.2448555.

[14] Kasinadhuni AK, Indahlastari A, Chauhan M, Scär M, Mareci TH, Sadleir RJ. Imaging of current flow in the human head during transcranial electrical therapy. Brain Stimul 2017;10:764–72. doi:10.1016/j.brs.2017.04.125.

[15] Göksu C, Hanson LG, Siebner HR, Ehses P, Scheffler K, Thielscher A. Human In-vivo Brain Magnetic Resonance Current Density Imaging (MRCDI). Neuroimage 2018;171:26–39.

[16] Scott GC, Joy MLG, Armstrong RL, Henkelman RM. Measurement of nonuniform current density by magnetic resonance. IEEE Trans Med Imaging 1991;10:362–74.

[17] Oh SH, Lee B Il, Woo EJ, Lee SY, Cho MH, Kwon O, et al. Conductivity and current density image reconstruction using harmonic Bz algorithm in magnetic resonance electrical impedance tomography. Phys Med Biol 2003;48:3101–16. doi:10.1088/0031-9155/48/19/001.

[18] Göksu C, Scheffler K, Ehses P, Hanson LG, Thielscher A. Sensitivity Analysis of Magnetic Field Measurements for Magnetic Resonance Electrical Impedance Tomography (MREIT). Magn Reson Med 2018;79:748–60. doi:10.1002/mrm.26727.

[19] Jaynes ET. Matrix treatment of nuclear induction. Phys Rev 1955;98:1099–105.

[20] Lee H, Jeong WC, Kim HJ, Woo EJ, Park J. Alternating steady state free precession for estimation of current-induced magnetic flux density: A feasibility study. Magn Reson Med 2016;75:2009–19.

[21] Nam HS, Kwon OI. Optimization of multiply acquired magnetic flux density B(z) using ICNE-Multiecho train in MREIT. Phys Med Biol 2010;55:2743–59.

[22] Friedman L, Glover GH. Report on a multicenter fMRI quality assurance protocol. J Magn Reson Imaging 2006;23:827–39. doi:10.1002/jmri.20583.

[23] Ida M, Wakayama T, Nielsen ML, Abe T, Grodzki DM. Quiet T1-Weighted Imaging Using PETRA : Initial Clinical Evaluation in Intracranial Tumor Patients. J Magn Reson Imaging 2015;41:447–53. doi:10.1002/jmri.24575.

[24] Dempsey MF, Condon B. Thermal injuries associated with MRI. Clin Radiol 2001;56:457–65. doi:10.1053/crad.2000.0688.

[25] Xu J, Moeller S, Auerbach EJ, Strupp J, Smith SM, Feinberg DA, et al. Evaluation of slice accelerations using multiband echo planar imaging at 3T. Neuroimage 2013;83:991–1001. doi:10.1016/j.neuroimage.2013.07.055.

[26] Dietrich O, Raya JG, Reeder SB, Reiser MF, Schoenberg SO. Measurement of signal-to-noise ratios in MR images: Influence of multichannel coils, parallel imaging, and reconstruction filters. J Magn Reson Imaging 2007;26:375–85. doi:10.1002/jmri.20969.

[27] Scott GC, Joy MLG, Armstrong RL, Henkelman RM. Sensitivity of magnetic-resonance current-density imaging. J Magn Reson 1992;97:235–54.

[28] Andersen M, Hanson LG, Madsen KH, Wezel J, Boer V, Van Der Velden T, et al. Measuring motion-induced B0-fluctuations in the brain using field probes. Magn Reson Med 2016;75:2020–30. doi:10.1002/mrm.25802.

[29] Kim HJ, Lee B Il, Cho Y, Kim YT, Kang BT, Park HM, et al. Conductivity imaging of canine brain using a 3 T MREIT system: postmortem experiments. Physiol Meas 2007;28:1341–53. doi:10.1088/0967-3334/28/11/002.

[30] Kim YT, Minhas AS, Meng Z, Kim HJ, Woo EJ. Conductivity imaging of human lower extremity using MREIT with multi-echo pulse sequence and 3 mA imaging current. 2011 8th Int Symp Noninvasive Funct Source Imaging Brain Hear 2011 8th Int Conf Bioelectromagn 2011:48–52. doi:10.1109/NFSI.2011.5936818.

[31] Jeong WC, Kim YT, Minhas a S, Lee TH, Kim HJ, Nam HS, et al. In vivo conductivity imaging of human knee using 3 mA injection current in MREIT. J Phys Conf Ser 2010;224:012148. doi:10.1088/1742-6596/224/1/012148.

[32] Jog M V, Smith RX, Jann K, Dunn W, Lafon B, Truong D, et al. In-vivo Imaging of Magnetic Fields Induced by Transcranial Direct Current Stimulation (tDCS) in Human Brain using MRI. Sci Rep 2016;6:34385. doi:10.1038/srep34385.

[33] Chauhan M, Indahlastari A, Kasinadhuni AK, Schar M, Mareci TH, Sadleir RJ. Low-Frequency Conductivity Tensor Imaging of the Human Head In Vivo Using DT-MREIT: First Study. IEEE Trans Med Imaging 2018;37:966–76. doi:10.1109/TMI.2017.2783348.

[34] Ehman RL, Felmlee JP. Adaptive technique for high-definition MR imaging of moving structures. Radiology 1989;173:255–63. doi:10.1148/radiology.173.1.2781017.

Figure 1

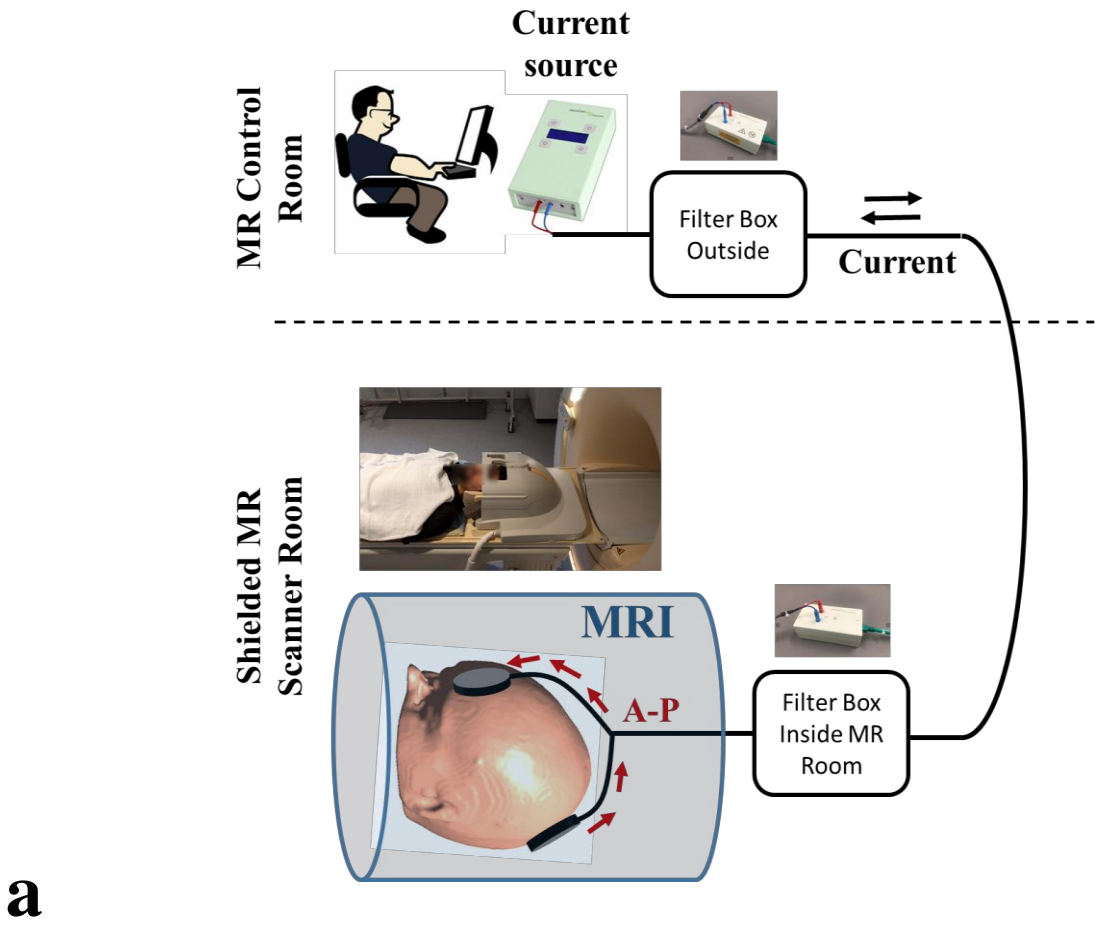
Current source
MR Control Room
Filter Box Outside
Current
Shielded MR Scanner Room
MRI
A-P
Filter Box Inside MR Room

a

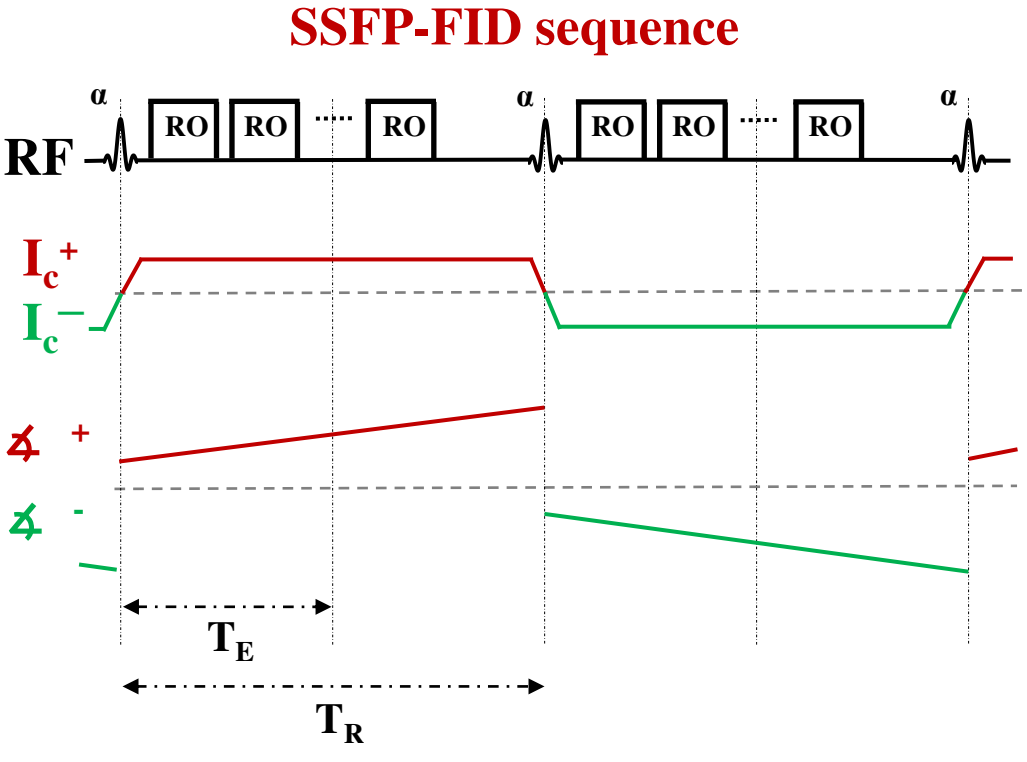
SSFP-FID sequence
α
RO
RF
I_c^+
I_c^-
T_E
T_R

b

Figure 2

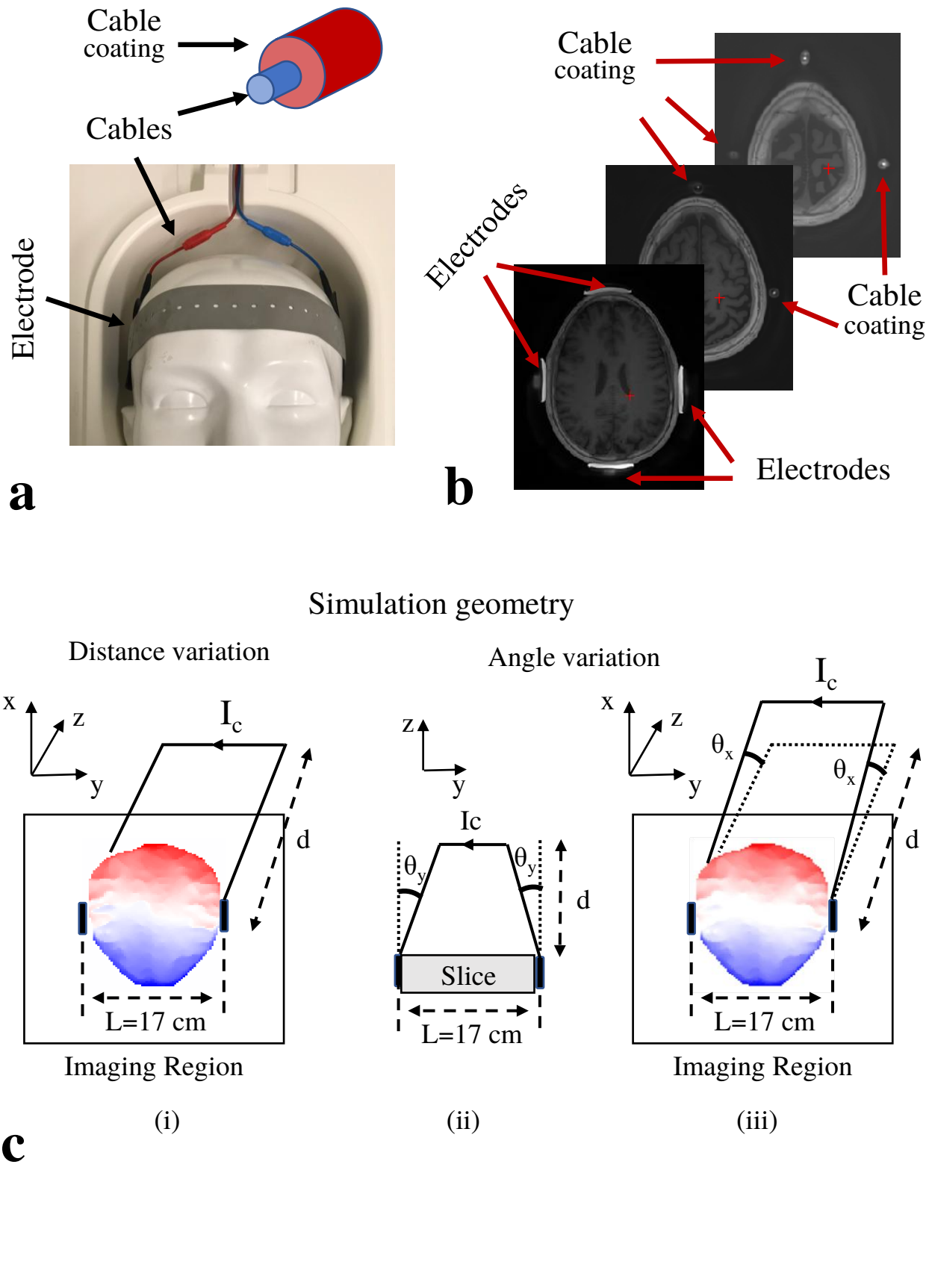
Cable
coating
Cables
Electrode
a
Cable
coating
Electrodes
Cable
coating
Electrodes
b
Simulation geometry
Distance variation
Angle variation
x
z
y
I_c
d
L=17 cm
Imaging Region
(i)
z
y
Ic
θ_y
θ_y
d
Slice
L=17 cm
(ii)
x
z
y
I_c
θ_x
θ_x
d
L=17 cm
Imaging Region
(iii)
c

Figure 3

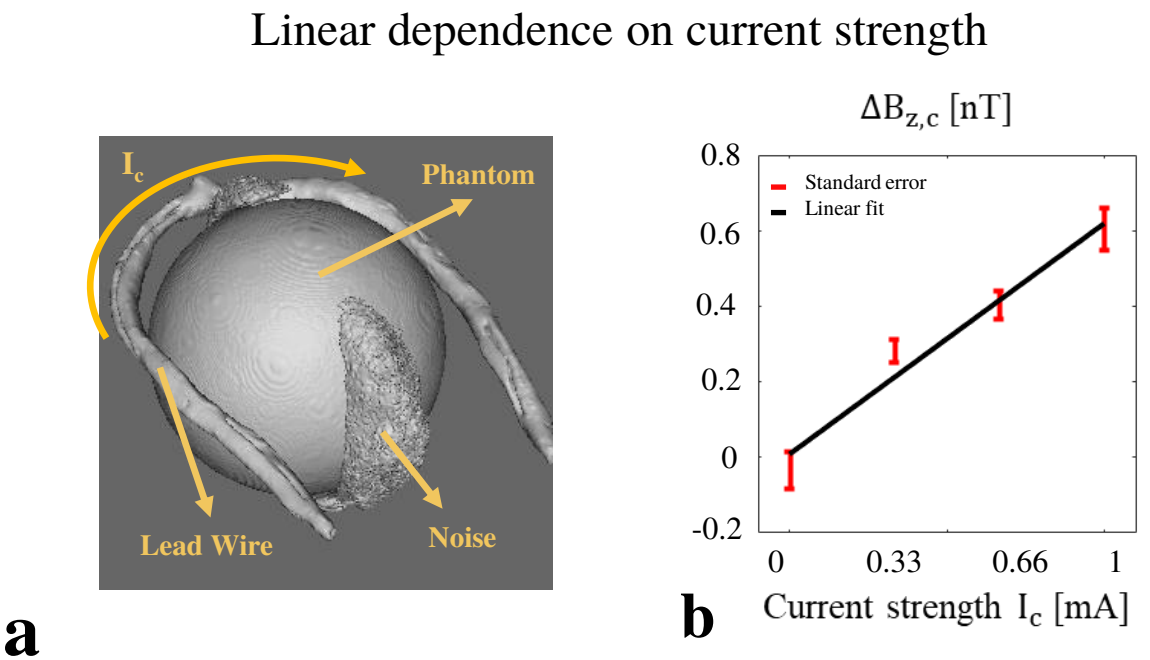
Linear dependence on current strength
I_c
Phantom
Lead Wire
Noise
a
$\Delta B_{z,c}$ [nT]
0.8
0.6
0.4
0.2
0
-0.2
Standard error
Linear fit
0
0.33
0.66
1
Current strength I_c [mA]
b

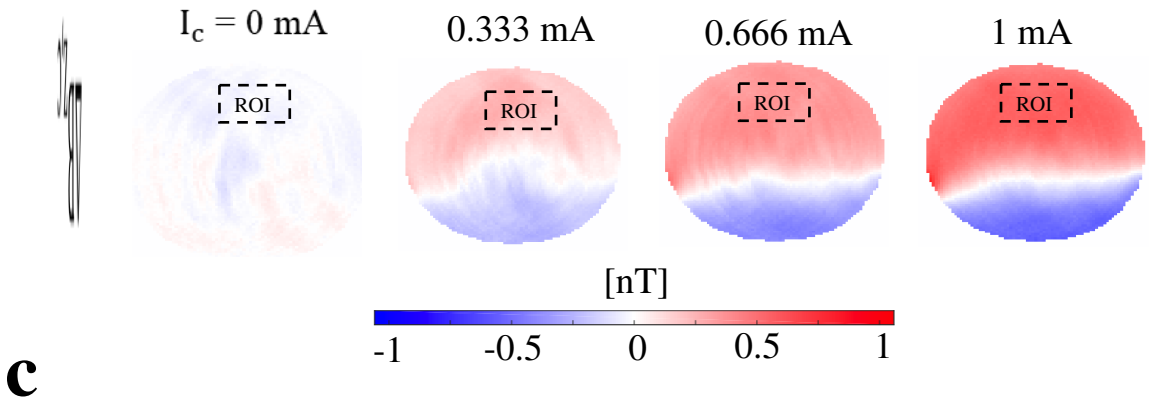
I_c = 0 mA
0.333 mA
0.666 mA
1 mA
ROI
ROI
ROI
ROI
[nT]
-1
-0.5
0
0.5
1
c

Figure 4

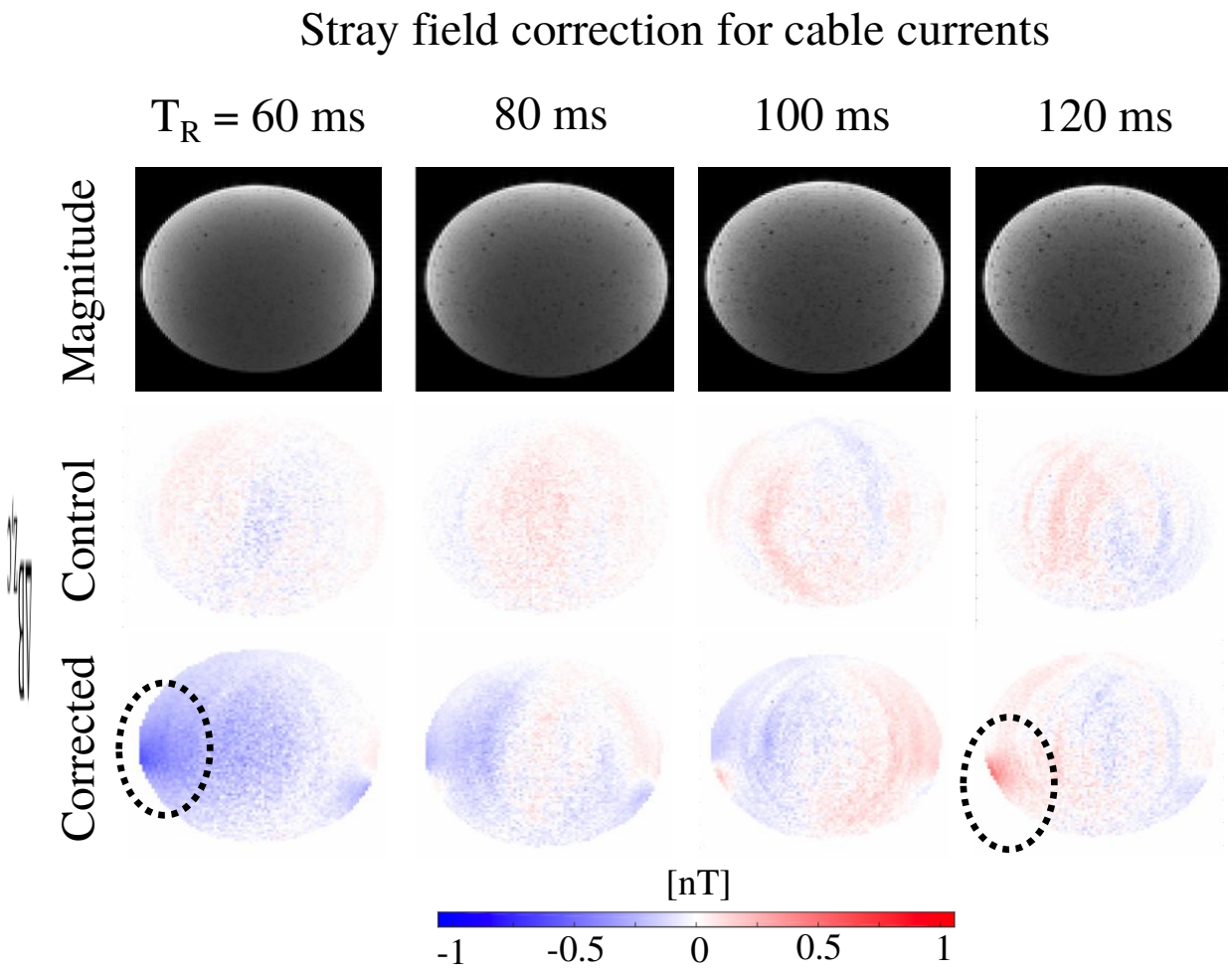
Stray field correction for cable currents
T_R = 60 ms
80 ms
100 ms
120 ms
Magnitude
Control
Corrected
[nT]
-1
-0.5
0
0.5
1

Figure 5

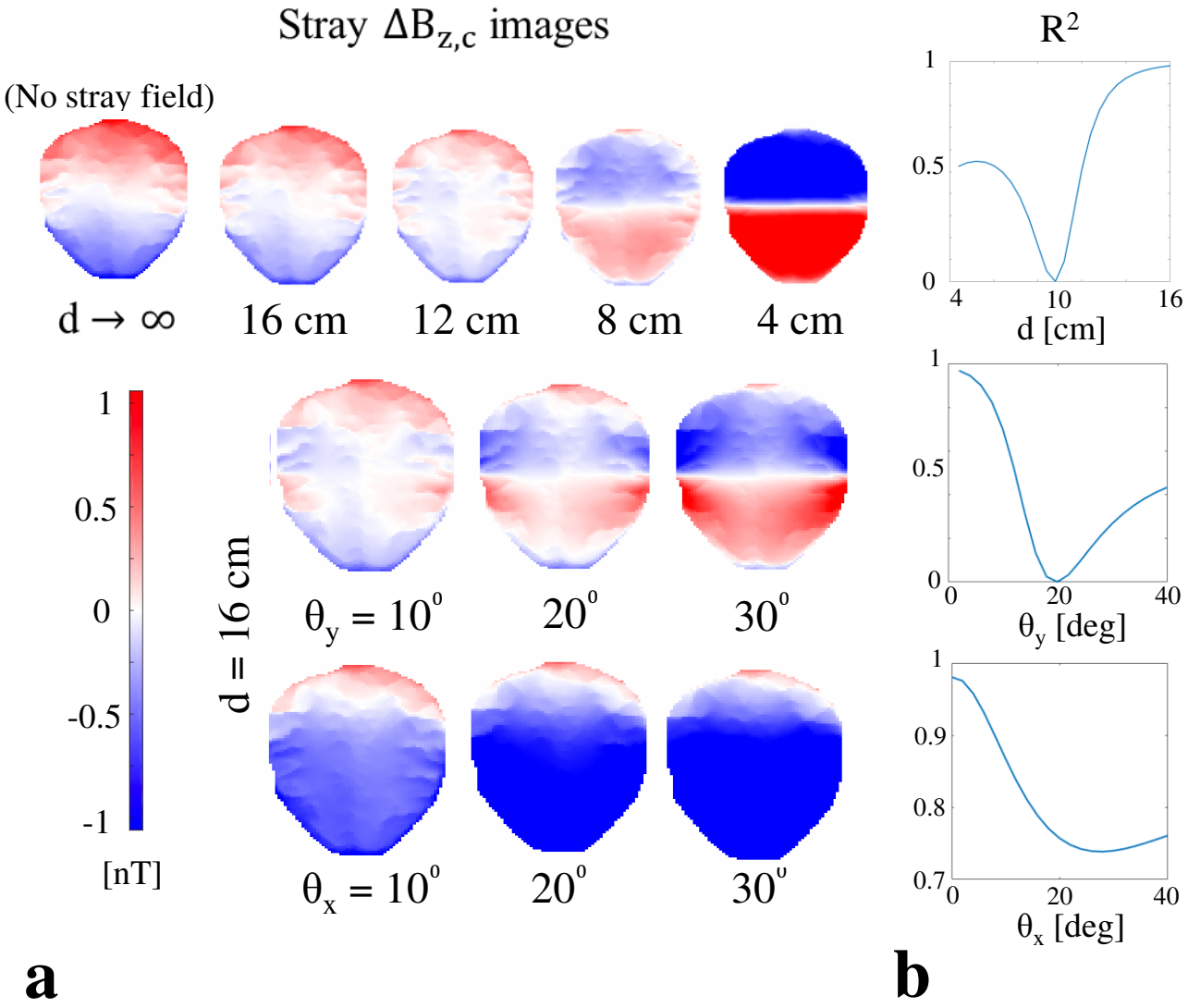
Stray ΔB$_{z,c}$ images
(No stray field)
d → ∞
16 cm
12 cm
8 cm
4 cm
1
0.5
0
-0.5
-1
[nT]
d = 16 cm
θ$_y$ = 10°
20°
30°
θ$_x$ = 10°
20°
30°
a
R^2
1
0.5
0
4
10
16
d [cm]
1
0.5
0
0
20
40
θ$_y$ [deg]
1
0.9
0.8
0.7
0
20
40
θ$_x$ [deg]
b

Figure 6

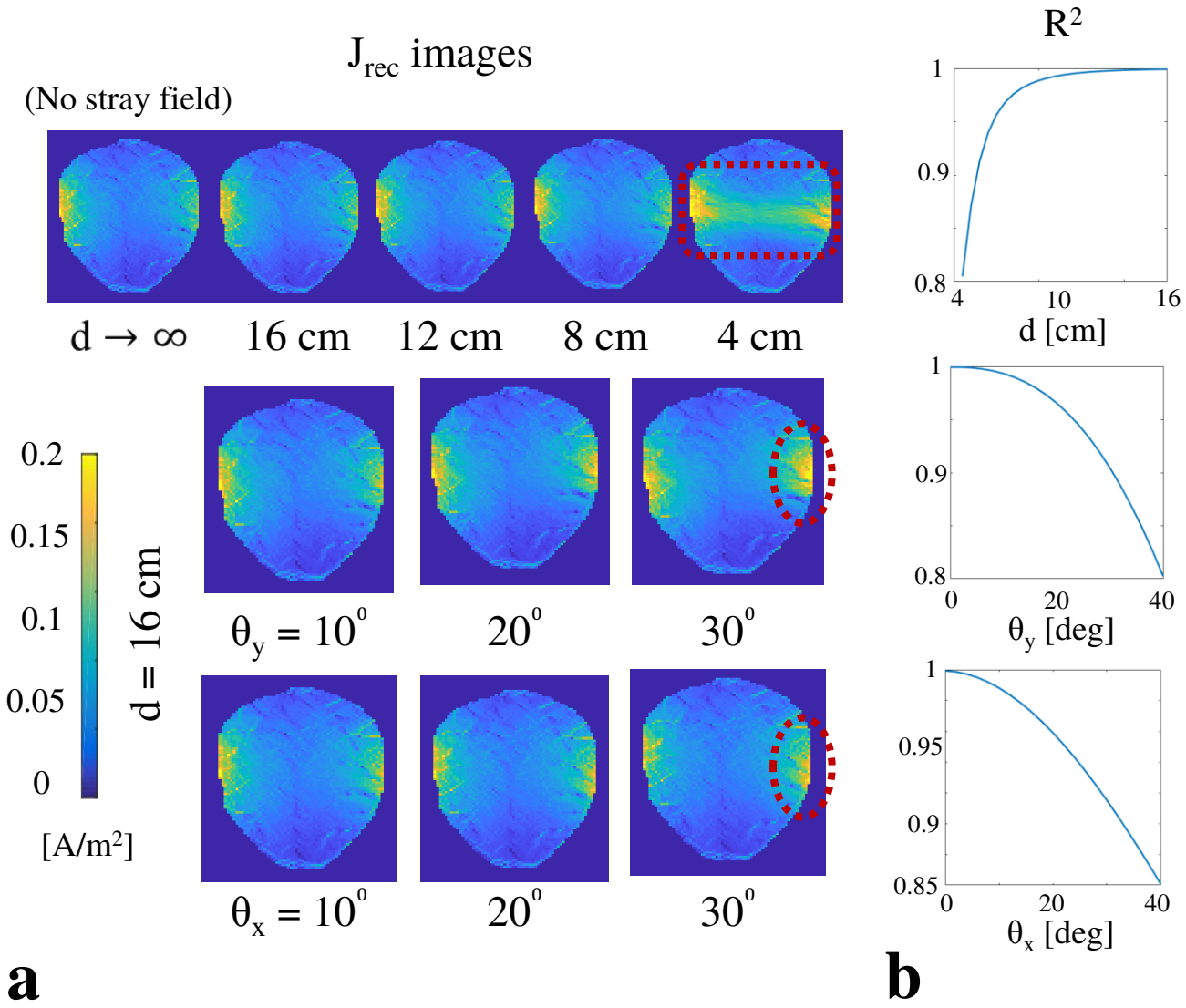
J_rec images
(No stray field)
d → ∞
16 cm
12 cm
8 cm
4 cm
0.2
0.15
0.1
0.05
0
[A/m²]
d = 16 cm
θy = 10°
20°
30°
θx = 10°
20°
30°
a
R²
1
0.9
0.8
4
10
16
d [cm]
1
0.9
0.8
0
20
40
θy [deg]
1
0.95
0.9
0.85
0
20
40
θx [deg]
b

Figure 7

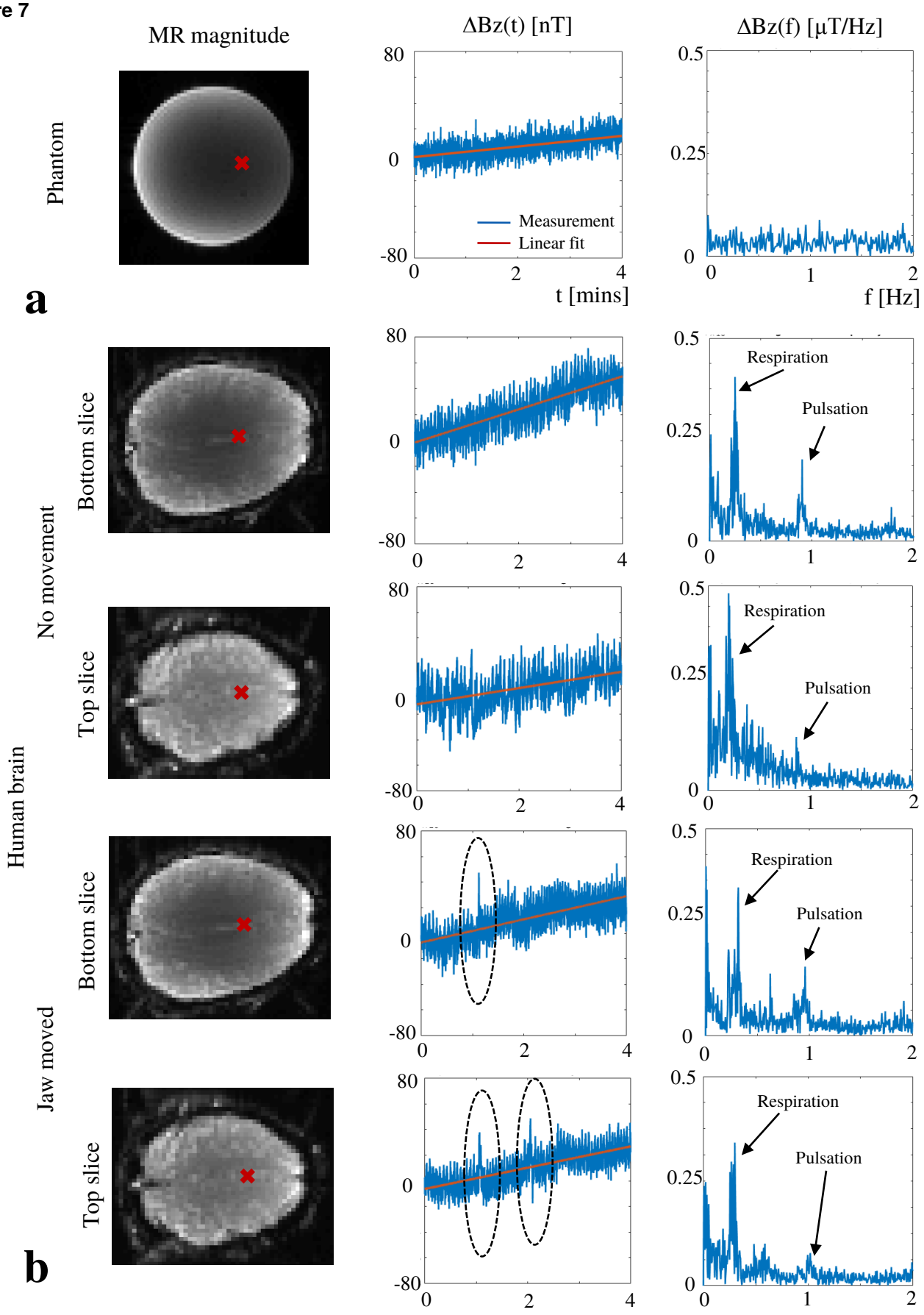
MR magnitude
ΔBz(t) [nT]
ΔBz(f) [μT/Hz]
Phantom
a
Measurement
Linear fit
t [mins]
f [Hz]
Human brain
No movement
Bottom slice
Top slice
Jaw moved
Bottom slice
Top slice
b
Respiration
Pulsation

The stray magnetic fields in Magnetic Resonance Current Density Imaging (MRCDI)

Cihan Göksu, Klaus Scheffler, Hartwig R. Siebner, Axel Thielscher, and Lars G. Hanson

Supplementary Material

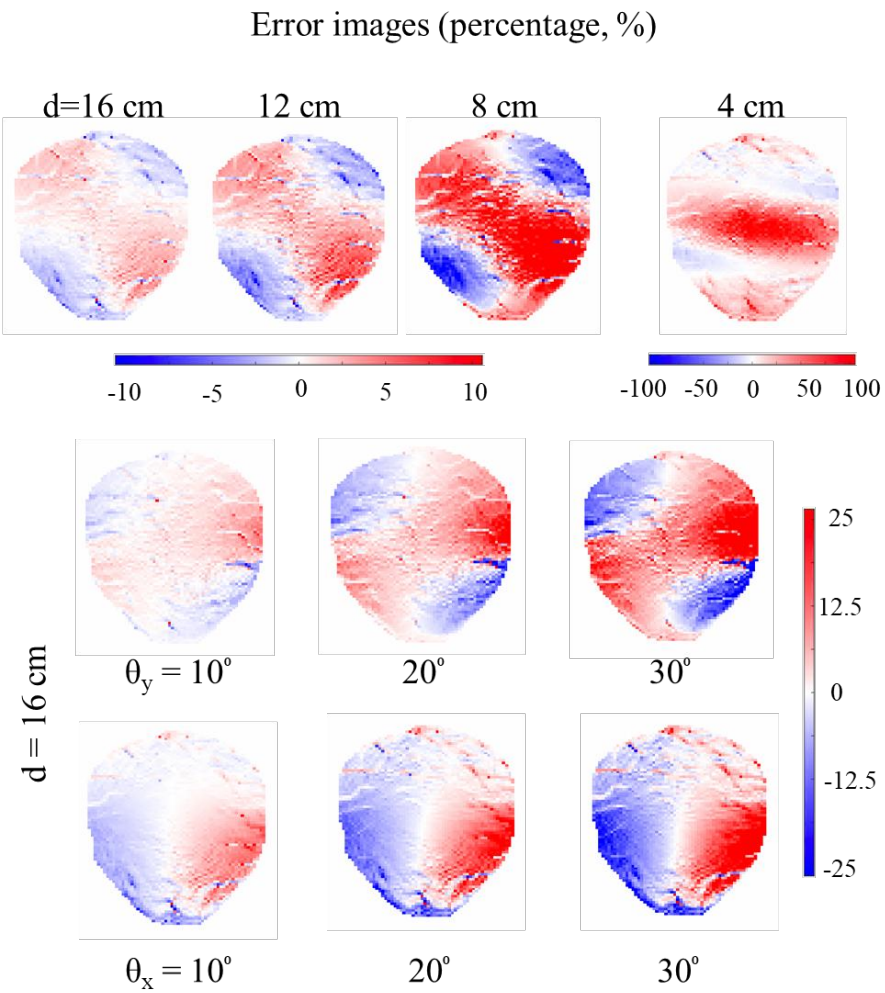

Supplementary Figure S1. Current density error images: Projected current density images were calculated from the field simulations in Fig. 5. The reconstructed current flow with no stray field was taken as reference and the error images were calculated accordingly. The error images demonstrate that the stray fields can cause significant under- or overestimation of the current flows depending on the positioning of the cables and the anatomical structures.

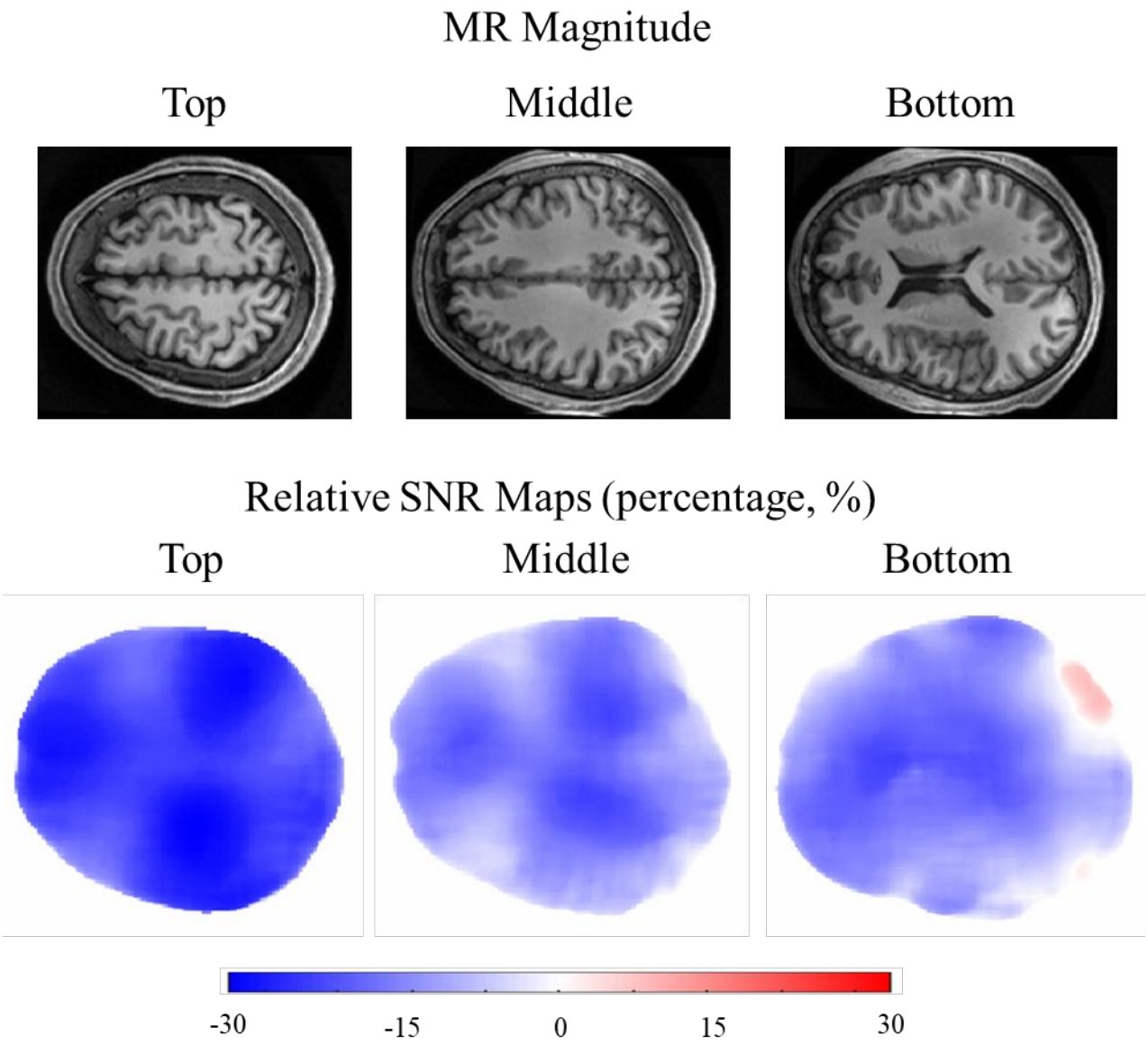

Supplementary Figure S2. MR magnitude images extracted from three different slices covering top, middle, and bottom part of the brain. No significant image artifacts were observed. The relative SNR maps were calculated as $\left({SNR_{offcenter}}/{SNR_{center}} - 1 \right) \times 100$ to represent the SNR compromise when off-centered coil positioning is chosen to minimize the stray field influences. In-plane median filtering of width 12 mm was applied to reduce errors due to imperfect co-registration.